



Endowing single-electron-trapped oxygen vacancy self-modified titanium dioxide with visible-light photocatalytic activity by grafting Fe(III) nanocluster

Haiyan Li ^{a,b}, Fengzhu Ren ^c, Jinfeng Liu ^a, Qinglong Wang ^a, Qiuye Li ^a, Jianjun Yang ^{a,*}, Yuanxu Wang ^{c,*}

^a Key Laboratory of Ministry of Education for Special Functional Materials, Henan University, Kaifeng 475004, China

^b College of Chemistry and Chemical Engineering, Henan University, Kaifeng 475004, China

^c Institute for Computational Materials Science, School of Physics and Electronics, Henan University, Kaifeng 475004, China



ARTICLE INFO

Article history:

Received 23 December 2014

Received in revised form 3 February 2015

Accepted 9 February 2015

Available online 10 February 2015

Keywords:

Nanotubular titanic acid

Titanium dioxide

Single-electron-trapped oxygen vacancy

Fe(III) nanocluster

Visible-light photocatalytic performance

ABSTRACT

Nanotubular titanic acid (denoted as NTA) was calcined in air to generate TiO_2 containing a large amount of single-electron-trapped oxygen vacancy (abridged as SETOV and denoted as V_0^\bullet). Resultant V_0^\bullet self-modified (or self-doped) TiO_2 (denoted as $\text{V}_0^\bullet\text{-TiO}_2$), visible light responsive but photocatalytically inactive under visible-light irradiation, was grafted with Fe(III) nanoclusters via an impregnation method to afford $\text{Fe(III)}\text{-V}_0^\bullet\text{-TiO}_2$ possessing visible-light photocatalytic activity. The photocatalytic performance of as-prepared $\text{Fe(III)}\text{-V}_0^\bullet\text{-TiO}_2$ photocatalysts was evaluated and compared with that of N-doped TiO_2 , and the experimental results were further discussed based on density functional theory calculations. Results reveal that grafting Fe(III) leads to nearly no changes in the crystalline structure as well as morphology and grain size of $\text{V}_0^\bullet\text{-TiO}_2$ but results in good visible-light photocatalytic performance for the photodegradation of gaseous propylene under visible-light irradiation. This is because the grafted Fe(III) nanoclusters act as efficient electron trapping centers to significantly enhance the electron transfer from oxygen vacancy state and the conduction band of TiO_2 to the adsorbed oxygen, thereby inducing the rapid separation of the photogenerated electrons and holes. Besides, the photocatalytic activity of $\text{Fe(III)}\text{-V}_0^\bullet\text{-TiO}_2$ photocatalysts is dependent on the dosage of grafted Fe(III), and it is critical to maintain a good matching between the energy level of V_0^\bullet and surface-grafted Fe(III) cocatalyst so as to facilitate fast and efficient charge transfer. Thanks to the good availability, low cost, and nontoxicity, Fe as the cocatalyst could find promising applications in the development of high-performance photocatalysts.

© 2015 Elsevier B.V. All rights reserved.

1. Introduction

Because of the high photocatalytic activity, low cost, easy availability and nontoxicity, titanium dioxide (TiO_2) has been extensively investigated since the discovery of the Fujishima–Honda effect in 1972 [1–3]. However, TiO_2 exhibits a wide band gap (3.20 eV for anatase and 3.00 eV for rutile) and can be only excited by ultraviolet (UV, covering less than 5% of the solar spectrum), which significantly limits its widespread applications. To extend the photo-responsive range of TiO_2 into visible spectral region, researchers have tried to dope TiO_2 with various anions (N, B, C, etc.)

[4–6] and cations (Cr, Fe, V, Zr, Mo, W, etc.) [7–12]. Unfortunately, doping strategy fails to provide high visible-light photocatalytic efficiency, although it does reduce the band gap of TiO_2 to some extent. This is because, on the one hand, anion doping forms isolated states above the valence band (abridged as VB) of TiO_2 , and the holes generated in these isolated states have lower oxidation power and mobility than those in the valence band [13,14]. On the other hand, cation doping tends to suffer from thermal instability and introduce deep impurity levels in the forbidden band of semiconductor photocatalysts, where they act as recombination centers and impair photocatalytic activity [2,3,15,16]. Similarly, coupling TiO_2 with narrow band gap semiconductors may also endow it with visible-light photocatalytic activity, because such a coupling strategy can generate photoexcited metal complex that is capable of giving an electron to the conduction band (abridged as CB) of TiO_2 under visible-light irradiation [17].

* Corresponding authors. Tel.: +86 371 23881358; fax: +86 371 23881358.

E-mail addresses: yangjianjun@henu.edu.cn (J. Yang), [\(Y. Wang\).](mailto:wangyx@henu.edu.cn)

Many recent investigations prove that TiO_2 grafted with metal ions (such as $\text{Cu}(\text{II})$, $\text{Fe}(\text{III})$, $\text{Cr}(\text{III})$, $\text{Ce}(\text{III})$) possesses higher visible-light photocatalytic activity than typical nitrogen-doped TiO_2 (denoted as $\text{N}-\text{TiO}_2$) and sensitized TiO_2 [18–26]. For example, Irie et al. fabricated $\text{Cu}(\text{II})$ -grafted visible-light responsive TiO_2 and WO_3 photocatalysts [18] and found that the as-fabricated photocatalysts exhibit higher photocatalytic oxidative activity than $\text{N}-\text{TiO}_2$ for the decomposition of gaseous 2-propanol under visible-light irradiation, because the electrons in the VB of TiO_2 can be directly excited to the surface grafted Cu^{2+} ions through interfacial charge transfer (denoted as IFCT) process thereby inducing multielectron oxygen reduction reaction [19]. Nakajima et al. prepared Cu -grafted TiO_2 -nanosheet thin films and proposed that the IFCT mechanism is also effective for nanosheet thin films [22]. Liu et al. found that surface grafting of $\text{Cu}(\text{II})$ endows photocatalytically inactive Ti^{3+} self-doped TiO_2 with good visible-light photocatalytic efficiency [21]. Yu et al. suggested that in $\text{Fe}(\text{III})$ -grafted TiO_2 , the direct IFCT from the VB of TiO_2 to Fe^{3+} also occurs, thereby resulting in a higher photocatalytic activity than Cu/TiO_2 [20]. Nishikawa et al. prepared $\text{Fe}(\text{III})$ -grafted TiO_2 and $\text{Fe}(\text{III})$ -grafted Ru-doped TiO_2 and clarified their photocatalytic reaction mechanisms under visible-light irradiation. They said that $\text{Ru}:\text{TiO}_2$ exhibits low photocatalytic activity under visible-light irradiation, because Ru^{3+} ions can act as a recombination center. Differing from $\text{Ru}:\text{TiO}_2$, $\text{Fe}/\text{Ru}:\text{TiO}_2$ allows the photoexcited electrons in Ru^{3+} ions to readily transfer to the grafted Fe^{3+} that is located at the surface of TiO_2 by indirect charge transfers, thereby preventing the recombination of photoexcited electrons and holes and leading to a higher photocatalytic activity [24]. Some researchers also reported that grafted metal ions can improve the visible-light photocatalytic performance of doped semiconductors [27–32]. For instance, Víctor et al. reported that $\text{Fe}(\text{III})$ -grafted S-doped TiO_2 exhibits quite high photoactivity under visible-light illumination for the degradation of dichloroacetic acid in the aqueous phase and NO_x in the gas phase [29]. Liu et al. found that $\text{Fe}(\text{III})$ grafting and doping results in obviously improved visible-light photocatalytic activity of TiO_2 [30,31]. Yu et al. said that grafting $\text{Fe}(\text{III})$ on the surface of $\text{TiO}_{2-x}\text{N}_x$ and AgBr leads to greatly enhanced photocatalytic performance for the decomposition of methyl orange under visible-light irradiation [32,33].

Previously we prepared anatase TiO_2 with a large amount of intrinsic defects: single-electron-trapped oxygen vacancy (abridged as SETOV and denoted as V_0^\bullet) by heat-treating nanotubular titanic acid ($\text{H}_2\text{Ti}_2\text{O}_4(\text{OH})_2$; denoted as NTA) at elevated temperature [34–41]. As-obtained V_0^\bullet self-modified TiO_2 (denoted as $\text{V}_0^\bullet-\text{TiO}_2$) exhibits a certain degree of visible-light absorption, due to the formation of a sub-band of the SETOV within the band gap of TiO_2 [39,40]. Unfortunately, $\text{V}_0^\bullet-\text{TiO}_2$ shows no photocatalytic activity under visible-light irradiation [42], because the V_0^\bullet is generated through the intra-layered dehydration of NTA [34] and is very stable and exists mainly in the bulk of TiO_2 . In other words, under visible-light irradiation, the excited electrons cannot be readily transferred to the surface of $\text{V}_0^\bullet-\text{TiO}_2$ owing to the absence of electron capture centers, which deteriorates the photocatalytic activity. To overcome this drawback, in the present research we utilize a simple impregnation method to prepare $\text{Fe}(\text{III})$ -grafted $\text{V}_0^\bullet-\text{TiO}_2$ (denoted as $\text{Fe}(\text{III})-\text{V}_0^\bullet-\text{TiO}_2$), hoping to acquire TiO_2 photocatalyst with greatly improved visible-light activity. This article reports the preparation and characterization of $\text{Fe}(\text{III})-\text{V}_0^\bullet-\text{TiO}_2$ photocatalysts and evaluation of their photocatalytic activities toward the decomposition of gaseous propylene (C_3H_6) under visible-light illumination. Here we selected $\text{Fe}(\text{III})$ as the to-be-grafted element, because it is easily available and exhibits low cost and nontoxicity as compared with noble metal nanoclusters such as Pt and Au.

2. Experimental

2.1. Synthesis of $\text{V}_0^\bullet-\text{TiO}_2$

$\text{V}_0^\bullet-\text{TiO}_2$ was prepared via a two-step route which involves the preparation of NTA through hydrothermal method and the calcination of NTA yielding anatase TiO_2 . Briefly, 3 g of commercially P25 TiO_2 powder was added into 300 mL of aqueous solution of NaOH (10 mol L⁻¹) under magnetic stirring. Resultant mixture was transferred into an autoclave and heated at 120 °C for 24 h to allow hydrothermal reaction affording a white precipitate. The white precipitate was washed repeatedly with deionized water and then immersed in HCl aqueous solution (0.1 mol L⁻¹) for 7 h under continuous magnetic stirring, followed by fully washing with deionized water to remove Cl^- . As-washed white precipitate was collected by filtration and dried at room temperature under vacuum, followed by grinding to yield NTA. As-obtained NTA was annealed at 600 °C for 2 h in a tubular furnace to afford $\text{V}_0^\bullet-\text{TiO}_2$, anatase TiO_2 with a large amount of SETOV.

2.2. Grafting of $\text{Fe}(\text{III})$ onto $\text{V}_0^\bullet-\text{TiO}_2$

An impregnation method reported elsewhere was applied to graft $\text{Fe}(\text{III})$ ion onto the surface of $\text{V}_0^\bullet-\text{TiO}_2$ [20]. Briefly, 1 g of $\text{V}_0^\bullet-\text{TiO}_2$ powder was dispersed in 10 mL of deionized water. Then $\text{FeCl}_3 \cdot 6\text{H}_2\text{O}$ was added into the $\text{V}_0^\bullet-\text{TiO}_2$ suspension at pre-set mass fractions (the mass fraction (wt%) of Fe to TiO_2 was fixed as 0.025, 0.050, 0.075, 0.100, 0.150, and 0.300) while HCl was dropped to adjust the pH value of the suspension to about 2. The suspension was finally heated at 90 °C for 1 h in a sealed round-bottom flask under stirring, followed by filtration with a membrane filter (0.2 mm), fully washing with deionized water (about 600 mL), drying at 110 °C for 24 h, and grinding in a mortar yielding $\text{Fe}(\text{III})-\text{V}_0^\bullet-\text{TiO}_2$ fine powder. $\text{Fe}(\text{III})$ -grafted NTA (denoted as $\text{Fe}(\text{III})$ -NTA) and $\text{Fe}(\text{III})$ -grafted P25 (denoted as $\text{Fe}(\text{III})$ -P25) were also prepared in the same manners and used for comparative studies. Moreover, $\text{N}-\text{TiO}_2$ and $\text{Fe}(\text{III})$ -doped TiO_2 (denoted as $\text{Fe}(\text{III})-\text{TiO}_2$) were also synthesized by calcining the mixture of urea and NTA at 600 °C for 2 h and the mixture of $\text{FeCl}_3 \cdot 6\text{H}_2\text{O}$ and NTA at 400 °C for 2 h so as to conduct comparative investigations.

2.3. Characterization

The crystal structure and morphology of as-prepared $\text{V}_0^\bullet-\text{TiO}_2$ and $\text{Fe}(\text{III})-\text{V}_0^\bullet-\text{TiO}_2$ were analyzed by powder X-ray diffraction (XRD; Bruker D8 advance diffractometer) and transmission electron microscopy (TEM; JEOL JEM-2010; accelerating voltage 200 kV). UV-vis light (abridged as UV-vis) absorption spectra were recorded in diffuse reflection pattern with a spectrophotometer (lambda950, PerkinElmer, USA) equipped with an integrating sphere assembly (wavelength range 200–800 nm, reference sample: BaSO_4). The specific surface area and pore volume of the products were determined by B-E-T (Brunauer, Emmett and Teller) method and B-J-H (Barrett, Joyner and Halenda) method, respectively, with which the N_2 adsorption-desorption isotherms were recorded with a Quadasorb SI-4 instrument. The composition of as-prepared products was analyzed by X-ray photoelectron spectroscopy (XPS; Kratos AXIS Ultra spectrometer) with monochromatized $\text{Al}-\text{K}\alpha$ ($h\nu = 1486.60$ eV) radiation as the excitation source; and the binding energy data were calibrated with reference to the C 1 s signal at 284.8 eV. Electron spin resonance (ESR) spectra were measured at 100 K under vacuum with an ESR spectrometer (Bruker EMX-8/2.7C).

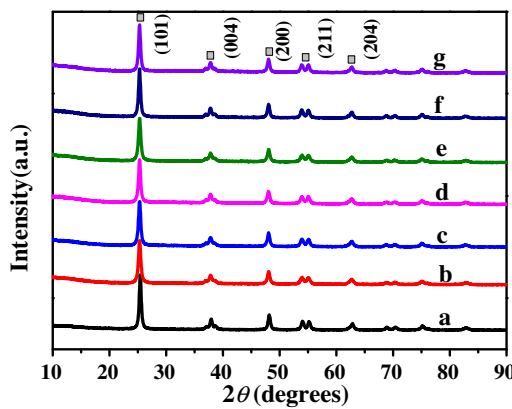


Fig. 1. XRD patterns of pure anatase $V_0^{\bullet}\text{-TiO}_2$ (a), 0.025% Fe(III)- $V_0^{\bullet}\text{-TiO}_2$ (b), 0.05% Fe(III)- $V_0^{\bullet}\text{-TiO}_2$ (c), 0.075% Fe(III)- $V_0^{\bullet}\text{-TiO}_2$ (d), 0.1% Fe(III)- $V_0^{\bullet}\text{-TiO}_2$ (e), 0.15% Fe(III)- $V_0^{\bullet}\text{-TiO}_2$ (f) and 0.3%Fe(III)- $V_0^{\bullet}\text{-TiO}_2$ (g).

2.4. Evaluation of photocatalytic activity

The photocatalytic activities of as-prepared photocatalysts were measured toward the decomposition of gaseous propylene under visible-light illumination from a 300 W Xe lamp equipped with a glass optical filter to cut off the short wavelength components ($\lambda \leq 420 \text{ nm}$). About 30 mg of the to-be-tested photocatalyst powder was uniformly spread on one side of a roughened glass plate (the irradiation area is about 7.8 cm^2) that was mounted in the middle of the flat quartz tube reactor. A water cell was inserted between the light source and the reactor to eliminate infrared light. The initial concentration of the feed gas, composed of gaseous propylene (C_3H_6) and air and stored in a high-pressure cylinder, is about $12 \mu\text{mol}$ ($\sim 600 \text{ ppmV}$), and its flow rate is about 150 mL h^{-1} . Prior to light irradiation, the to-be-tested samples were kept in the dark for about 2 h to allow C_3H_6 to achieve the absorption-desorption equilibrium on the photocatalyst surface. It was assumed that the adsorption of C_3H_6 gas onto the photocatalyst surfaces was completed when the C_3H_6 concentration remained a constant, and then the Xe lamp was turned on to initiate the photocatalytic reaction. During the reaction process, the concentration of C_3H_6 produced was monitored with a gas chromatograph (Shimadzu GC-9A) equipped with a flame ionization detector and a GDX-502 column. The photo-oxidation removal rate of C_3H_6 was determined as $(C_0 - C)/C_0 \times 100\%$, where C_0 refers to the initial concentration of C_3H_6 and C refers to the concentration of C_3H_6 produced at different photocatalytic reaction durations.

2.5. Calculation of density of states (DOS)

The plane-wave-based spin polarized density functional theory (denoted as DFT) calculations for pure anatase TiO_2 and $V_0^{\bullet}\text{-TiO}_2$ were performed with the Vienna ab initio simulation package (VASP) [43,44]. The projector augmented wave method (PAW) [45] was chosen to elucidate the core-valence interactions, and the general gradient approximation (GGA) [46] in the scheme of Perdew–Burke–Ernzerhof (PBE) [47] was adopted to describe the exchange and correlation potential. The GGA+U method was used to calculate the DOS of TiO_2 and $V_0^{\bullet}\text{-TiO}_2$. The U parameter ($U_{\text{eff}} = 5.8 \text{ eV}$ [48] for the Ti 3d orbit) was used to reach an agreement with the experimental band gap of anatase TiO_2 . Anatase TiO_2 was modeled with a $2 \times 2 \times 2$ super cell containing 32 Ti atoms and 64 O atoms. A singly ionized oxygen vacancy (i.e., V_0^{\bullet}) state was created by removing one oxygen atom from the TiO_2 model. The cutoff energy for the plane-wave basis is set as 500 eV in the present calculations. Several convergence tests in the k -point sampling were

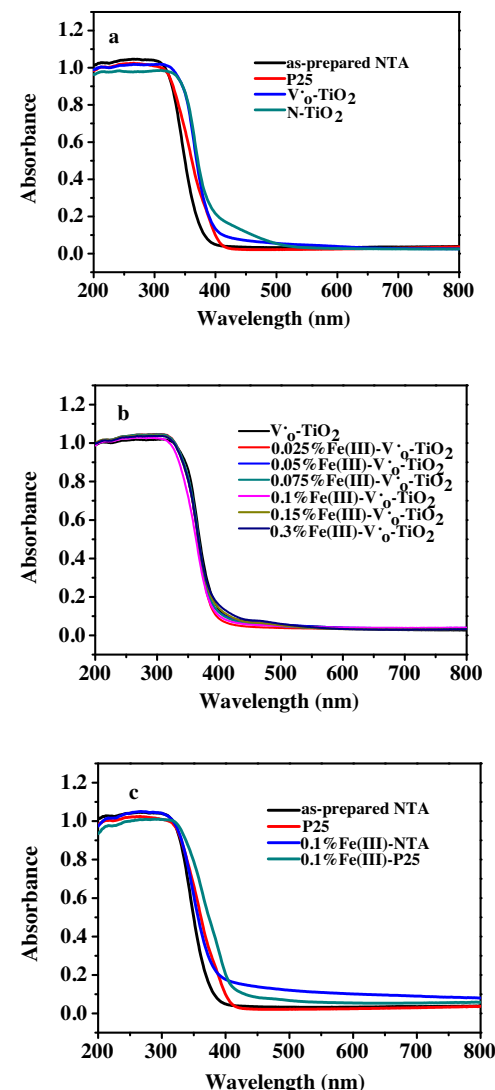


Fig. 2. UV-vis diffuse reflectance spectra of as-prepared NTA, P25, $V_0^{\bullet}\text{-TiO}_2$, Fe(III)- $V_0^{\bullet}\text{-TiO}_2$, $N\text{-TiO}_2$, 0.1%Fe(III)-NTA and 0.1%Fe(III)-P25.

performed, and Monkhorst–Pack k -point mesh of $3 \times 3 \times 1$ was used for electronic property calculations, and it was found to be sufficient to reach convergence of the super cells. The calculations were performed with relaxation of both atomic positions and lattice parameters so as to find the most stable lattice structure. The convergence of the total energy within 10^{-7} eV is set as the ending criterion for electronic self-consistent interactions.

3. Results and discussion

3.1. Structural characterization

Fig. 1 shows the XRD patterns of $V_0^{\bullet}\text{-TiO}_2$ and various Fe(III)- $V_0^{\bullet}\text{-TiO}_2$ samples. It is seen that $V_0^{\bullet}\text{-TiO}_2$ is composed of anatase TiO_2 , and the presence of V_0^{\bullet} can be verified by relevant ESR spectra (see below). Besides, Fe(III)- $V_0^{\bullet}\text{-TiO}_2$ samples with different dosages of grafted Fe(III) retain the crystalline structure of anatase TiO_2 , which indicates that surface-grafted Fe(III) ions have no effect on the anatase-rutile phase transformation. Moreover, no obvious diffraction peaks of iron compounds are observed, possibly because of the low grafting content of Fe(III) ions.

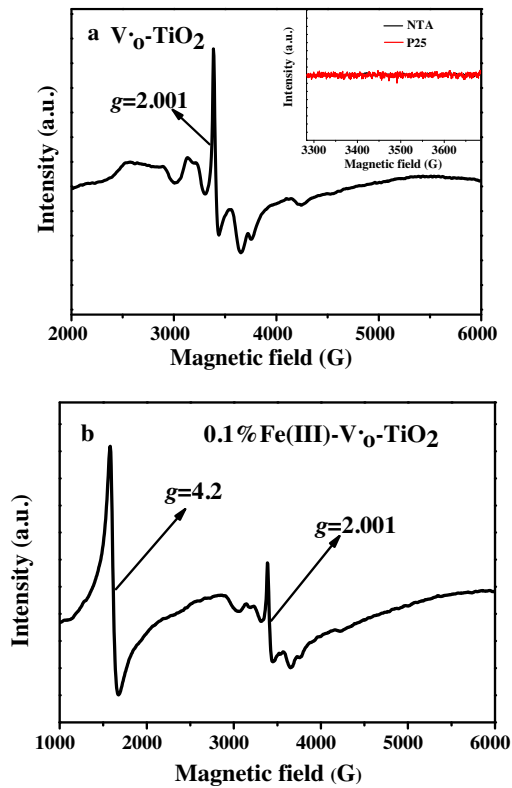


Fig. 3. ESR spectra of $V_0^{\bullet}\text{-TiO}_2$ and $0.1\%\text{Fe(III)}\text{-}V_0^{\bullet}\text{-TiO}_2$ measured at 100 K in vacuum. The inset shows ESR spectra of as-obtained NTA and P25 under the same condition.

3.2. UV-vis diffuse reflectance spectra

Fig. 2a presents the UV-vis diffuse reflectance spectra of as-prepared NTA, P25, $V_0^{\bullet}\text{-TiO}_2$ and N-TiO₂ reference. As-prepared NTA shows absorption thresholds at ~ 380 nm, which corresponds to its interband transition, and its band gap is 3.26 eV. The absorption onset of P25 at ~ 410 nm corresponds to its interband transition, and its band gap is 3.00 eV. Compared with NTA, the absorption of P25 tends to be extended to a longer wavelength region to some extent, possibly because NTA possesses a larger band gap than P25. Besides, $V_0^{\bullet}\text{-TiO}_2$ exhibits stronger visible-light absorptions than NTA and P25, because $V_0^{\bullet}\text{-TiO}_2$ contains a large amount of SETOV which locates at 0.90–1.20 eV below the CB bottom of TiO₂ (see theoretical calculation section), and can form an intra-band within the band gap of TiO₂, and thereby obviously improving the visible-light absorption [39,40]. In contrast, N-TiO₂ shows much stronger visible-light absorptions than that of $V_0^{\bullet}\text{-TiO}_2$ in the wavelength range of 400–550 nm. For N-TiO₂, the SETOV is also present below the CB bottom of TiO₂ due to its preparation process proceeded the same thermal dehydration of the nanotubular titanic acid. Except for the contribution of V_0^{\bullet} , the energy level of doped-N element is relatively closer to the VB of TiO₂. The combined action between the two is favorable for the electron transitions from the midgap electronic states of the doped-N to the TiO₂ conduction band and for the absorbing of energies far below the TiO₂ band gap, thereby inducing stronger absorption than $V_0^{\bullet}\text{-TiO}_2$.

Fig. 2b shows the UV-vis diffuse reflectance spectra of Fe(III)- $V_0^{\bullet}\text{-TiO}_2$ samples. It can be seen that the various Fe(III)- $V_0^{\bullet}\text{-TiO}_2$ samples show the absorptions in the range of ca. 350–550 nm, and that are similar to that of $V_0^{\bullet}\text{-TiO}_2$. Particularly, Fe(III)- $V_0^{\bullet}\text{-TiO}_2$ samples containing less than 0.3% of grafted Fe(III) do not show obvious absorption attributed to the interfacial charge

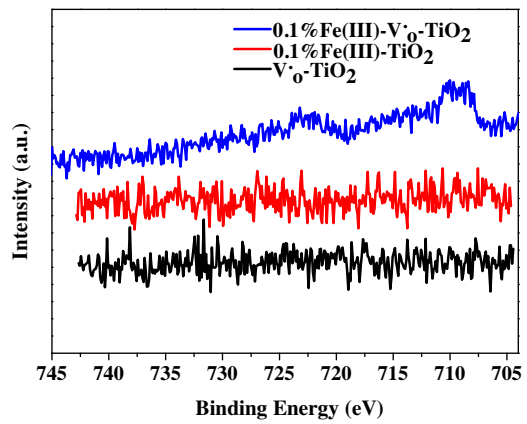


Fig. 4. Fe 2p core-level XPS spectra of $V_0^{\bullet}\text{-TiO}_2$, $0.1\%\text{Fe(III)}\text{-TiO}_2$ and $0.1\%\text{Fe(III)}\text{-}V_0^{\bullet}\text{-TiO}_2$.

transfer (IFCT) from the valence band of TiO₂ to the Fe(III) ions (ca. 410–580 nm) [20], which coincides with our theoretical analysis and indicates that the absorption of these Fe(III)- $V_0^{\bullet}\text{-TiO}_2$ samples is mainly attributed to the contribution of V_0^{\bullet} formed during NTA annealing. According to relevant theoretical calculation results, the intra-band formed by V_0^{\bullet} is located at 0.90–1.20 eV below the conduction band of TiO₂. In the meantime, the redox potential of $\text{Fe}^{3+}/\text{Fe}^{2+}$ for the surface grafted Fe(III) ions is 0.771 V (vs normal hydrogen electrode (NHE) at pH 0), which is very close to the energy level of V_0^{\bullet} and is located above it. Therefore, it can be concluded that the valence band electrons of TiO₂ may be first excited to the energy states of interband levels contributed by V_0^{\bullet} and then transferred to grafted Fe(III) ions on TiO₂ surface. Namely, surface-grafted Fe(III) nanoclusters and SETOV have nearly identical energy levels, which may further contribute to enhancing the photocatalytic activity under visible-light irradiation (see below). In addition, the IFCT from the valence band of TiO₂ to Fe(III) ions cannot be excluded, but it is not enough to produce efficient visible-light absorption.

The UV-vis diffuse reflectance spectra of $0.1\%\text{Fe(III)}\text{-NTA}$ and $0.1\%\text{Fe(III)}\text{-P25}$ were also measured and compared with those of as-obtained NTA and P25 to further verify that the light absorption of Fe(III)- $V_0^{\bullet}\text{-TiO}_2$ is mainly attributed to V_0^{\bullet} . As shown in Fig. 2c, NTA and P25 show only absorptions attributed to the band gap excitation at wavelengths below 380 nm (for NTA) and 410 nm (for P25). However, both $0.1\%\text{Fe(III)}\text{-NTA}$ and $0.1\%\text{Fe(III)}\text{-P25}$ show obvious visible-light absorption at 410–550 nm and 425–520 nm, respectively, due to the IFCT process from the valence band of TiO₂ to the Fe(III) ions. This demonstrates that both Fe(III)-NTA and Fe(III)-P25 undergo IFCT process, and the visible-light absorption of Fe(III)- $V_0^{\bullet}\text{-TiO}_2$ should be mainly ascribed to V_0^{\bullet} .

3.3. ESR analysis and XPS analysis

To prove the existence of V_0^{\bullet} and investigate the state of Fe ions in Fe(III)-grafted photocatalysts, we recorded low temperature ESR spectra at 100 K in vacuum. As shown in Fig. 3a, NTA and P25 are ESR-silent (inset in Fig. 3a), which indicates that they do not contain unpaired electrons. However, a clear ESR signal centered at $g=2.003$ can be observed for $V_0^{\bullet}\text{-TiO}_2$ obtained by annealing NTA in air. In the past decade, we have investigated the properties of nanotubular titanic acid systematically [34,39,40,49]. It is found that, when nanotubular titanic acid is either annealed in air or dehydrated in vacuum, a sharp ESR signal centered at $g=2.003$ can be detected, which is assigned to a bulk defect, namely, single-electron-trapped oxygen vacancy (SETOV). In the present study, it is noted that the V_0^{\bullet} was formed by the intra-layered

dehydration of nanotubular titanic acid, which is different from Ti^{3+} mostly formed by undergoing vacuum or reducing atmosphere (such as H_2) treatments. Moreover, the ESR signal peak of paramagnetic Ti^{3+} center usually shows broad absorption peak at $g = 1.96 - 1.99$ [50]. So, the observed sharp ESR signal peak should be attributed to single-electron-trapped oxygen vacancy, while the weak satellite peaks around the center peak can be ascribed to the perturbation peaks resulting from the strong interaction between the single-electron-trapped oxygen vacancies. The above analysis indicates that $\text{V}_0^{\bullet}\text{-TiO}_2$ contains intrinsic solid defects (i.e., V_0^{\bullet}), and there is no Ti^{3+} species in the obtained samples. Furthermore, aside from the signal of V_0^{\bullet} , 0.1%Fe(III)- $\text{V}_0^{\bullet}\text{-TiO}_2$ presents another large ESR signal centered around $g = 4.200$ at low magnetic field of about 1600 G (Fig. 3b); and this paramagnetic signal peak, assigned to Fe^{3+} located in a strongly distorted rhombic environment [51,52], confirms that Fe(III) species are successfully grafted onto the surface of $\text{V}_0^{\bullet}\text{-TiO}_2$ but not enter into the bulk of TiO_2 . The reason lies in that the ESR peak of doped-Fe should appear at $g = 1.995 - 2.000$ if Fe ions substitute Ti ions in octahedral environment [53–55].

Fig. 4 shows the Fe 2p core-level XPS spectra of $\text{V}_0^{\bullet}\text{-TiO}_2$, Fe(III)- TiO_2 and Fe(III)- $\text{V}_0^{\bullet}\text{-TiO}_2$. It is seen that Fe signal is only observed for Fe(III)- $\text{V}_0^{\bullet}\text{-TiO}_2$, which again proves that Fe(III) nanoclusters, reportedly with distorted amorphous FeO(OH) -like structure [20], are successfully grafted onto the surface of TiO_2 . According to the XPS results, the real amount of Fe(III) loading can be calculated to be ca. 0.35 at% for the sample 0.1%Fe(III)- $\text{V}_0^{\bullet}\text{-TiO}_2$. After the mixture of NTA and $\text{FeCl}_3\cdot 6\text{H}_2\text{O}$ (the Fe to TiO_2 mass fraction of the mixture is the same as that of 0.1%Fe(III)- $\text{V}_0^{\bullet}\text{-TiO}_2$) is heated at high temperature, resultant 0.1%Fe(III)-doped TiO_2 does

not show the XPS signal of iron, which means that in this case Fe(III) ions are doped into TiO_2 lattice during high temperature treatment, and the intensity of the surfaced-doped Fe ions is too low to be detected by XPS.

3.4. TEM analysis

The TEM image of NTA, the precursor for fabricating TiO_2 , is shown in Fig. 5a. The orthorhombic system NTA has a layered structure. The distance between the adjacent layers of NTA is about 0.8 nm; the V_0^{\bullet} is generated through the intra-layered dehydration of NTA in association with the crystal form transition from orthorhombic system to anatase phase under heat treatment [34], and as-formed V_0^{\bullet} mostly exists in the bulk and exhibits a good stability. After NTA is heated at 600 °C in air for 2 h, its layered structure is broken to generate $\text{V}_0^{\bullet}\text{-TiO}_2$ nanoparticles with an average grain size of about 12 nm (Fig. 5b). The HRTEM image indicates that $\text{V}_0^{\bullet}\text{-TiO}_2$ exhibits a well-resolved anatase (101) lattice plane with a *d*-spacing of 0.348 (Fig. 5c), which well coincides with relevant XRD result. In the meantime, the morphology and particle size of Fe(III)- $\text{V}_0^{\bullet}\text{-TiO}_2$ are similar to those of $\text{V}_0^{\bullet}\text{-TiO}_2$, which reveals that the introduction of Fe(III) ions onto the TiO_2 surface does not change the morphology and particle size of the photocatalyst (Fig. 5d). However, the TEM image provides little detailed information about the microstructure of Fe(III) nanoclusters grafted on TiO_2 surface, largely because the content of grafted Fe(III) nanoclusters is too low.

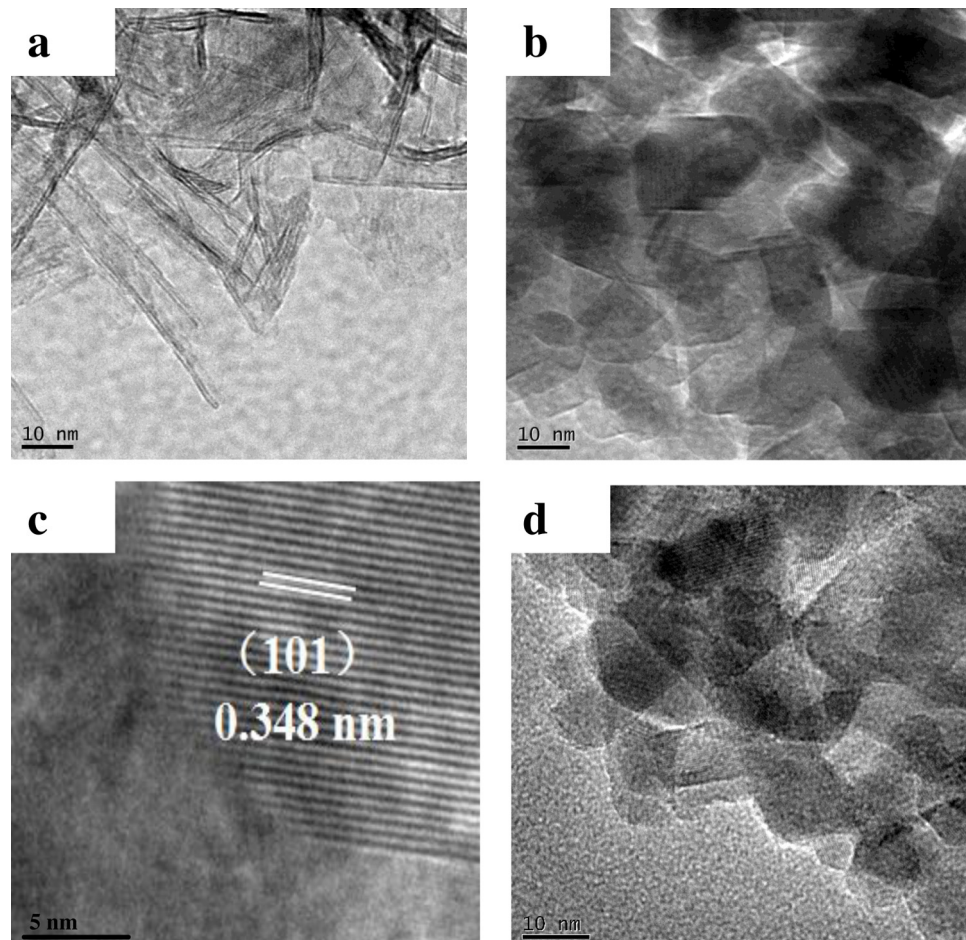
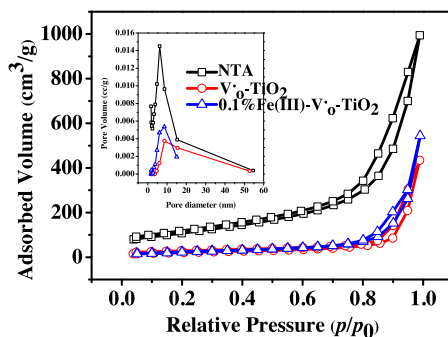


Fig. 5. TEM images of as-prepared NTA (a), $\text{V}_0^{\bullet}\text{-TiO}_2$ (b), 0.1%Fe(III)- $\text{V}_0^{\bullet}\text{-TiO}_2$ (d) and high-resolution TEM (HRTEM) image of $\text{V}_0^{\bullet}\text{-TiO}_2$ (c).

Table 1Physicochemical properties of NTA, P25, V_0^{\bullet} – TiO_2 , Fe(III)– V_0^{\bullet} – TiO_2 , N– TiO_2 , 0.1%Fe(III)–NTA, 0.1%Fe(III)–P25 and 0.1%Fe(III)– TiO_2 .

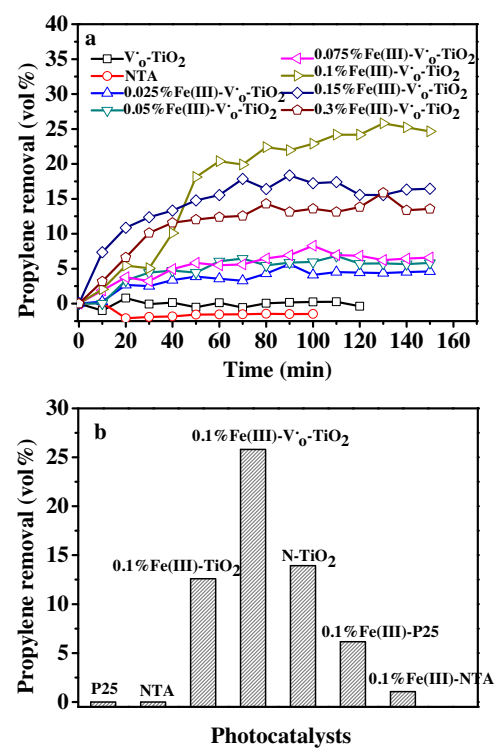
Catalysts	BET surface area (m^2/g)	Pore volume (cc/g)	Pore size (nm)	Band gap (eV)
NTA	390.6	1.538	6.2	3.26
P25	54.4	0.516	15.3	3.20
V_0^{\bullet} – TiO_2	73.7	0.671	8.7	2.84
0.025%Fe(III)– V_0^{\bullet} – TiO_2	91.2	0.456	8.6	2.91
0.05%Fe(III)– V_0^{\bullet} – TiO_2	82.8	0.581	8.6	2.90
0.075%Fe(III)– V_0^{\bullet} – TiO_2	82.9	0.528	8.8	2.89
0.1%Fe(III)– V_0^{\bullet} – TiO_2	89.6	0.841	8.6	2.91
0.15%Fe(III)– V_0^{\bullet} – TiO_2	75.2	0.606	8.8	2.89
0.3%Fe(III)– V_0^{\bullet} – TiO_2	77.4	0.862	8.7	2.86
N– TiO_2	49.1	0.361	8.8	2.73
0.1%Fe(III)–NTA	348.7	1.431	6.2	2.84
0.1%Fe(III)–P25	54.4	0.488	15.6	2.80
0.1%Fe(III)– TiO_2	172.5	0.490	1.7	2.87

**Fig. 6.** Nitrogen adsorption–desorption isotherms and pore size distribution curves (inset) of as-prepared NTA, V_0^{\bullet} – TiO_2 and 0.1%Fe(III)– V_0^{\bullet} – TiO_2 .

3.5. BET surface area and pore distributions analysis

The surface area and porosity of various products, calculated from the N_2 adsorption–desorption isotherms, are listed in **Table 1**. As-prepared NTA exhibits the largest surface area ($390.6\text{ m}^2/\text{g}$) among various photocatalysts, which well corresponds to its nanotubular structure. V_0^{\bullet} – TiO_2 has a much smaller surface area ($73.7\text{ m}^2/\text{g}$) than NTA, which is attributed to the destruction of the nanotubular structure of NTA upon heating at elevated temperature in air. Besides, the pore volume of V_0^{\bullet} – TiO_2 is smaller than that of NTA, while the pore size of the former is larger than that of the latter. This indicates that, during the formation of V_0^{\bullet} upon calcining NTA in air, an acute local structural collapse takes place in association with the enlargement of the mesoporous structure, which well coincides with the morphology change from nanotube to nanoparticle. Moreover, the surface areas of Fe(III)– V_0^{\bullet} – TiO_2 samples are slightly larger than that of V_0^{\bullet} – TiO_2 , which implies that Fe(III) grafting has few influence on the morphology and grain size of V_0^{\bullet} – TiO_2 , as evidenced by relevant TEM analysis. Furthermore, Fe(III)– V_0^{\bullet} – TiO_2 photocatalysts containing less than 0.1% of grafted Fe(III) ion exhibit similar surface areas, possibly because they allow a high level of dispersion of Fe(III) nanoclusters on V_0^{\bullet} – TiO_2 . When the mass fraction of grafted Fe(III) is above 0.1%, the surface areas of Fe(III)– V_0^{\bullet} – TiO_2 photocatalysts tends to decrease to some extent, possibly because of the aggregation of Fe(III) nanoparticles on TiO_2 surface in the form of $FeO(OH)$ -like amorphous clusters. Viewing that the various Fe(III)– V_0^{\bullet} – TiO_2 photocatalysts exhibit similar pore size to that of V_0^{\bullet} – TiO_2 , we can infer that Fe(III) nanoparticles are not incorporated into the pores of V_0^{\bullet} – TiO_2 .

As a typical example, **Fig. 6** presents the N_2 adsorption–desorption isotherms of as-prepared NTA, V_0^{\bullet} – TiO_2 and 0.1%Fe(III)– V_0^{\bullet} – TiO_2 , where the inset refers to corresponding pore size distribution curves. It can be seen that all the three photocatalysts exhibit similar type-IV adsorption–desorption isotherms

**Fig. 7.** (a) Visible-light photocatalytic activities of as-prepared NTA, V_0^{\bullet} – TiO_2 and Fe(III)– V_0^{\bullet} – TiO_2 . (b) Comparative studies of visible-light photocatalytic activities of P25, NTA, 0.1%Fe(III)– TiO_2 , 0.1%Fe(III)– V_0^{\bullet} – TiO_2 , N– TiO_2 , 0.1%Fe(III)–P25 and 0.1%Fe(III)–NTA.

with an H3 hysteresis loop in a relative pressure range of 0.60–1.00, which indicates that they are of mesoporous structure [56]. The pore size distribution profiles also confirm that as-prepared NTA, V_0^{\bullet} – TiO_2 and Fe(III)– V_0^{\bullet} – TiO_2 are of mesoporous structure (the data of Fe(III)– V_0^{\bullet} – TiO_2 samples with different Fe(III) dosages are omitted).

3.6. Photocatalytic activities of Fe(III)– V_0^{\bullet} – TiO_2

Fig. 7a shows the effect of the dosage of grafted Fe(III) ion on the photocatalytic activity of V_0^{\bullet} – TiO_2 . As-prepared NTA has no any photocatalytic activity for the photo-oxidation of propylene, which corresponds to its large band gap of 3.26 eV and zero visible-light absorption. V_0^{\bullet} – TiO_2 does not exhibit any photocatalytic activity either, though it contains a large amount of V_0^{\bullet} within the band gap and possesses significantly improved visible-light absorption. This is because the photocatalytic process is very complex and can be impacted by many factors such as light absorption

properties and separation efficiency of photogenerated charge carriers. Although V_0^\bullet extends the absorption of V_0^\bullet -TiO₂ into the visible-light region, the excited electrons cannot be transferred onto the photocatalyst surface and trapped timely, due to the lack of efficient electron trapping centers in association with the increase of the e^- - h^+ recombination rate. As a result, V_0^\bullet -TiO₂ exhibits no photocatalytic activity for the photodegradation of propylene. Differing from V_0^\bullet -TiO₂ and NTA, Fe(III)- V_0^\bullet -TiO₂ samples can effectively accelerate the photodegradation of propylene under visible-light irradiation, which implies that Fe(III) grafting greatly boosts the visible-light photocatalytic capability of V_0^\bullet -TiO₂. Besides, the photocatalytic activity of Fe(III)- V_0^\bullet -TiO₂ samples increases with the increase of mass fraction of Fe(III) and reaches the maximum at a Fe(III) dosage of 0.1 wt%, beyond which the photocatalytic activity begins to decrease therewith. This might be because, at a lower content of grafted Fe(III) ion, no enough Fe(III) nanoclusters function to accept the electrons derived from the valence band of TiO₂ and V_0^\bullet , and some entrapped electrons tend to be recombined thereby resulting in decreased photocatalytic activity. As the mass fraction of grafted Fe(III) exceeds 0.1%, further increase in the dosage of the Fe(III) ion leads to a decrease in the removal rate of propylene, due to the “quenching” effect of the generated holes and Fe(II) [20]. Namely, at the high dosage of the Fe(III) ion, the recombination possibility of the generated holes and Fe(II) would be increased before holes are encountered with propylene and oxygen molecules are reduced by Fe(II). Moreover, since Fe(III)- V_0^\bullet -TiO₂ samples exhibit similar light absorption performance (Fig. 2b) and surface area (Table 1), the difference in their photocatalytic activities should not be attributed to the difference in their light absorption performance and surface area.

N-TiO₂ is generally considered as an excellent visible-light photocatalyst, especially for photodegradation of organic pollutants, and P25 is a benchmark photocatalyst that works under UV irradiation. Fig. 7b shows the photocatalytic activities of N-TiO₂ and P25 for comparisons. P25 does not exhibit any photocatalytic activity, because it is non-responsive to visible light. The photocatalytic activity of N-TiO₂ with strong visible-light absorption is lower than that of 0.1%Fe(III)- V_0^\bullet -TiO₂, except for the effect of the smaller surface area (49.1 m²/g) than 0.1%Fe(III)- V_0^\bullet -TiO₂ (89.6 m²/g), most probably because the former is liable to strong recombination of photogenerated charges [57]. The photocatalytic activity of 0.1%Fe(III)-TiO₂ (i.e., Fe(III)doped TiO₂) with the larger surface area (172.5 m²/g) is also lower than that of 0.1%Fe(III)- V_0^\bullet -TiO₂. Maybe because the actual visible-light absorption of 0.1%Fe(III)-NTA and 0.1%Fe(III)-P25 derived from IFCT (Fig. 2c) remains very limited and weak, the two samples also show low photocatalytic activity toward propylene removal though 0.1%Fe(III)-NTA catalyst exhibits a large surface area of 348.7 m²/g. The above analysis indicates that Fe(III) grafted V_0^\bullet -TiO₂ samples possess high photocatalytic activity toward propylene removal, and meanwhile it also implies that the surface area is not the predominant factor of the present photocatalytic systems.

3.7. Theoretical calculation and photocatalytic mechanism of Fe(III)- V_0^\bullet -TiO₂

All Fe(III)- V_0^\bullet -TiO₂ samples do not have obvious IFCT-derived absorption, which implies that they are dominated by an indirect charge transfer. Namely, the electrons in the valence band of TiO₂ are initially excited to the energy level formed by V_0^\bullet and then transferred to grafted Fe(III) ion but not directly transferred to the grafted Fe(III) ion. Compared to Fe(III)-NTA and Fe(III)-P25 possessing visible-light absorption derived from IFCT, Fe(III)- V_0^\bullet -TiO₂ photocatalysts exhibit higher photocatalytic activities, which means that the electrons in the V_0^\bullet states could be quickly and efficiently transferred to surface grafted Fe(III) ion

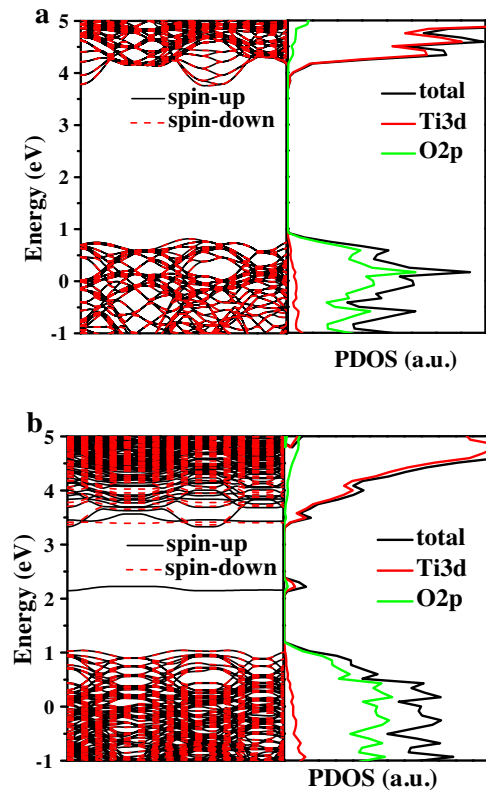


Fig. 8. Band structure plots and partial density of states for pure anatase TiO₂ (a) and V_0^\bullet -TiO₂ at 1.04 at % oxygen vacancy concentration (b).

cocatalyst, thereby causing multielectron reduction of adsorbed oxygen molecules. These observations reminds us that the energy level formed by V_0^\bullet could be closer to the potential of Fe^{3+}/Fe^{2+} redox couple in the surface grafted Fe(III) ions, and the two have a good energy level matching. In other words, grafted Fe(III) cocatalyst in combination with V_0^\bullet jointly functions to enhance the photocatalytic activity by way of effectively consuming photogenerated electrons via efficient interfacial charge transfer and multielectron reduction reactions.

To verify the abovementioned supposition, we conducted DFT calculations of anatase TiO₂ and V_0^\bullet -TiO₂. Fig. 8a presents the band structure and density of state of pure anatase TiO₂. It is seen that the calculated band gap of pure anatase TiO₂ is about 2.90 eV, being consistent with the experimental one (3.20 eV). Besides, O 2p states dominate at the top of the valence band while Ti 3d states dominate at the bottom of the conduction band. When V_0^\bullet is introduced into TiO₂ lattice, a localized impurity state located at 0.90–1.20 eV below the conduction band of TiO₂ appears (Fig. 8b). It is very interesting that, compared to the redox potential of Fe^{3+}/Fe^{2+} ($E^\circ = 0.771$ V vs NHE at pH = 0) [30] in the surface grafted Fe(III) ions, the energy state formed by V_0^\bullet is very close to the redox potential of Fe^{3+}/Fe^{2+} and is located below it, meaning that the electrons on the oxygen vacancy states can be easily transferred to the Fe(III) cocatalyst. So, under visible-light irradiation, the electrons can be transferred from the valence band of TiO₂ to the impurity state formed by V_0^\bullet and further to the grafted Fe ions, thereby quenching direct IFCT absorption. Fig. 8b displays the DOS of V_0^\bullet -TiO₂, where an isolated inter-band level of V_0^\bullet is responsible for inducing the visible-light absorption of V_0^\bullet -TiO₂, which agrees well with corresponding experimentally determined absorption under UV-vis irradiation. To our surprise, theoretical calculations also proves that V_0^\bullet -TiO₂ has no photocatalytic activity, and a relative deep energy level is introduced by V_0^\bullet within the band gap and it readily becomes

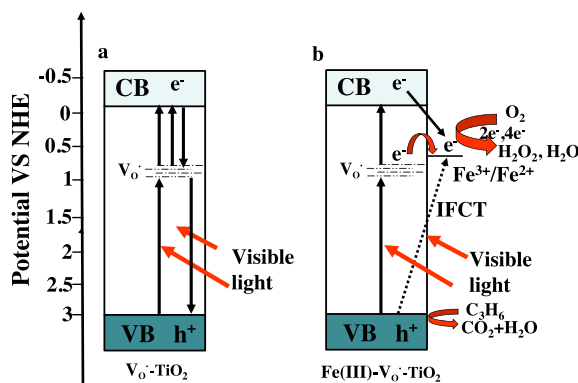


Fig. 9. Proposed photocatalytic mechanisms for $\text{Fe}(\text{III})-\text{V}_0^{\bullet}-\text{TiO}_2$.

carrier recombination center thereby impairing photocatalytic activity, as shown in Fig. 9a.

After the grafting of $\text{Fe}(\text{III})$ cocatalyst on the surface of $\text{V}_0^{\bullet}-\text{TiO}_2$, the resulting $\text{Fe}(\text{III})-\text{V}_0^{\bullet}-\text{TiO}_2$ photocatalyst showed a higher photocatalytic activity compared to $\text{V}_0^{\bullet}-\text{TiO}_2$. To understand the roles of the loaded $\text{Fe}(\text{III})$ cocatalyst, combining with DFT calculation results, a possible photocatalytic mechanism for the enhanced photocatalytic activity was proposed in Fig. 9b. Under visible-light irradiation, the electrons in oxygen defect sites can be efficiently transferred to the surface $\text{Fe}(\text{III})$ nanoclusters due to the matching energy level, and unoccupied states are formed upon the transfer of the electrons in oxygen vacancy states. Upon the formation of the unoccupied states, the electrons in the valence band of TiO_2 are excited to the unoccupied sites and subsequently transferred to the $\text{Fe}(\text{III})$ nanoclusters or partly excited to the conduction band of TiO_2 . In the meantime, a part of photogenerated electrons in the conduction band may also be transferred to the grafted $\text{Fe}(\text{III})$ ion on TiO_2 surface thereby affording $\text{Fe}(\text{II})$ ion upon acceptance of a photogenerated electron by $\text{Fe}(\text{III})$ ion. As-formed $\text{Fe}(\text{II})$ ions are unstable and tend to be oxidized by oxygen molecule under ambient conditions yielding $\text{Fe}(\text{III})$ ion again. In other words, the $\text{Fe}(\text{III})$ ions can be well recovered via the effective oxidation of $\text{Fe}(\text{II})$ ions by oxygen. However, in the absence of surface $\text{Fe}(\text{III})$ cocatalyst, the unoccupied oxygen defect sites act as electron traps and lead to easy recombination of the photogenerated charge carriers (Fig. 9a). Therefore, $\text{V}_0^{\bullet}-\text{TiO}_2$ does not exhibit photocatalytic activity under visible-light irradiation, though it has visible-light absorption. Differing from $\text{V}_0^{\bullet}-\text{TiO}_2$, $\text{Fe}(\text{III})-\text{V}_0^{\bullet}-\text{TiO}_2$ allows the photoinduced electrons to be quickly transferred to surface $\text{Fe}(\text{III})$ nanoclusters with the assistance of oxygen vacancy with an identical energy level with $\text{Fe}(\text{III})$ nanoclusters and efficiently consumed by taking part in the oxygen reduction process, thereby decreasing the recombination rate of photogenerated charges both in the bulk and on the surface and further leading to a significant enhancement of photocatalytic activity of $\text{Fe}(\text{III})-\text{V}_0^{\bullet}-\text{TiO}_2$. While the more holes in the valence band in combination with reactive hydroxyl radicals (OH^{\bullet}) functions to accelerate the decomposition of propylene. Moreover, the multielectron oxygen reduction process ($\text{O}_2 + 2\text{e}^- + 2\text{H}^+ = \text{H}_2\text{O}_2$) produces H_2O_2 that may also take part in the oxidation reaction thereby contributing to the accelerated decomposition of propylene. As a result, $\text{Fe}(\text{III})-\text{V}_0^{\bullet}-\text{TiO}_2$ exhibits enhanced photocatalytic activity than $\text{V}_0^{\bullet}-\text{TiO}_2$. Though the direct IFCT process from the valence band of TiO_2 to $\text{Fe}(\text{III})$ nanoclusters is not obvious, it can also contribute to the enhanced photocatalytic activity. On the basis of the above results, it can be strongly demonstrated that $\text{Fe}(\text{III})$ can be act as an efficient cocatalyst to greatly improve the visible-light photocatalytic activity of $\text{V}_0^{\bullet}-\text{TiO}_2$. It could be worth noting that a good matching between the energy level of V_0^{\bullet} and surface-grafted $\text{Fe}(\text{III})$ ion is critical for the fast and efficient charge transfer in the

present system, while indirect charge transfer seems to be more beneficial to photocatalysis than direct charge transfer.

4. Conclusions

Amorphous $\text{Fe}(\text{III})$ nanoclusters were grafted onto the surfaces of TiO_2 via a simple and economical method to convert photochemically inactive $\text{V}_0^{\bullet}-\text{TiO}_2$ into an efficient visible-light-sensitive photocatalyst. Experimental measurements in combination with theoretical analysis indicate that the intra-band formed by V_0^{\bullet} is below the conduction band of TiO_2 and close to the redox potential of $\text{Fe}^{3+}/\text{Fe}^{2+}$. Under visible-light irradiation, the electrons in oxygen vacancy states may be transferred to the surface $\text{Fe}(\text{III})$ nanoclusters fast and efficiently, while the electrons in the valence band of TiO_2 can be transferred indirectly. Namely, the surface grafted $\text{Fe}(\text{III})$ amorphous nanoclusters as the cocatalyst for efficient oxygen reduction can consume photoinduced electrons and suppress the recombination of electron-hole pairs at the oxygen vacancy states, while the holes with strong oxidation power produced in the valence band of TiO_2 and H_2O_2 produced via multielectron oxygen reduction process may also accelerate the decomposition of propylene. Therefore, $\text{Fe}(\text{III})-\text{V}_0^{\bullet}-\text{TiO}_2$ exhibits better photocatalytic oxidative activity for the photodegradation of C_3H_6 than $\text{N}-\text{TiO}_2$. Thanks to its good availability, low cost and nontoxicity, $\text{Fe}(\text{III})$ ion as the cocatalyst of wide band gap semiconductor could find promising application in the development of high-performance photocatalysts.

Author contributions

The manuscript was written through contributions of all authors. All authors have given approval to the final version of the manuscript. Haiyan Li and Fengzhu Ren contributed equally.

Acknowledgements

This work is financially supported by the Ministry of Education of China (program for Changjiang Scholars and Innovation Research Team in Universities, grant No. PCSIRT1126) and the National Natural Science Foundation of China (grant Nos. 21103042, 20973054, and 21203054).

References

- [1] A. Fujishima, K. Honda, Nature 238 (1972) 37–38.
- [2] M.R. Hoffmann, S.T. Martin, W. Choi, D.W. Bahnemann, Chem. Rev. 95 (1995) 69–96.
- [3] X.B. Chen, S.S. Mao, Chem. Rev. 107 (2007) 2891–2959.
- [4] R. Asahi, T. Morikawa, T. Ohwaki, K. Aoki, Y. Taga, Science 293 (2001) 269–271.
- [5] W. Zhao, W.H. Ma, C.C. Chen, J.C. Zhao, Z.G. Shuai, J. Am. Chem. Soc. 126 (2004) 4782–4783.
- [6] I.-C. Kang, Q.W. Zhang, S. Yin, T. Sato, F. Saito, Appl. Catal. B 80 (2008) 81–87.
- [7] G.K. Larsen, R. Fitzmorris, J.Z. Zhang, Y.P. Zhao, J. Phys. Chem. C 115 (2011) 16892–16903.
- [8] Q.P. Wu, R.V.-D. Krol, J. Am. Chem. Soc. 134 (2012) 9369–9375.
- [9] J.-C.-S. Wu, C.-H. Chen, J. Photochem. Photobiol. A 163 (2004) 509–515.
- [10] P.E. Lippens, A.V. Chadwick, A. Weibel, R. Bouchet, P. Knauth, J. Phys. Chem. C 112 (2008) 43–47.
- [11] S. Wang, L.N. Bai, H.M. Sun, Q. Jiang, J.S. Lian, Powder Technol. 244 (2013) 9–15.
- [12] H.P. Xu, J.H. Liao, S. Yuan, Mater. Res. Bull. 51 (2014) 326–331.
- [13] R. Asahi, T. Morikawa, T. Ohwaki, K. Aoki, Y. Taga, Science 293 (2001) 269–271.
- [14] H. Irie, Y. Watanabe, K. Hashimoto, J. Phys. Chem. B 107 (2003) 5483–5486.
- [15] T.L. Thompson, J.T. Yates, Chem. Rev. 106 (2006) 4428–4453.
- [16] J.G. Highfield, P. Pichat, New. J. Chem. 13 (1989) 61–66.
- [17] W. Zhou, H.G. Fu, K. Pan, C.G. Tian, Y. Qu, P.P. Lu, C.-C. Sun, J. Phys. Chem. C 112 (2008) 19584–19589.
- [18] H. Irie, S. Miura, K. Kamiya, K. Hashimoto, Chem. Phys. Lett. 457 (2008) 202–205.
- [19] H. Irie, K. Kamiya, T. Shibanuma, S. Miura, D.A. Tryk, T. Yokoyama, K. Hashimoto, J. Phys. Chem. C 113 (2009) 10761–10766.

[20] H. Yu, H. Irie, Y. Shimodaira, Y. Hosogi, Y. Kuroda, M. Miyauchi, K. Hashimoto, *J. Phys. Chem. C* 114 (2010) 16481–16487.

[21] M. Liu, X.Q. Qiu, M. Miyauchi, K. Hashimoto, *Chem. Mater.* 23 (2011) 5282–5286.

[22] A. Nakajima, Y. Akiyama, S. Yanagida, T. Koike, T. Isobe, Y. Kameshima, K. Okada, *Mater. Lett.* 63 (2009) 1699–1701.

[23] Y. Nosaka, S. Takahashi, H. Sakamoto, A.Y. Nosaka, *J. Phys. Chem. C* 115 (2011) 21283–21290.

[24] M. Nishikawa, Y. Mitani, Y. Nosaka, *J. Phys. Chem. C* 116 (2012) 14900–14907.

[25] H. Irie, S. Miura, R. Nakamura, K. Hashimoto, *Chem. Lett.* 37 (2008) 252–253.

[26] R. Nakamura, A. Okamoto, H. Osawa, H. Irie, K. Hashimoto, *J. Am. Chem. Soc.* 129 (2007) 9596–9597.

[27] S. Anandan, M. Miyauchi, *Electrochemistry* 79 (2011) 842–844.

[28] S. Anandan, N. Ohashi, M. Miyauchi, *Appl. Catal. B* 100 (2010) 502–509.

[29] V.M. Menéndez-Flores, D.W. Bahnemann, T. Ohno, *Appl. Catal. B* 103 (2011) 99–108.

[30] M. Liu, X.Q. Qiu, M. Miyauchi, K. Hashimoto, *J. Am. Chem. Soc.* 135 (2013) 10064–10072.

[31] M. Miyauchi, X.Q. Qiu, M. Lin, K. Hashimoto, *Photocatalysis* 35 (2011) 56–59.

[32] X.F. Wang, K. Wang, K.W. Feng, F. Chen, H.G. Yu, J.G. Yu, *J. Mol. Catal. A* 391 (2014) 92–98.

[33] H.G. Yu, L.L. Xu, P. Wang, X.F. Wang, J.G. Yu, *Appl. Catal. B* 144 (2014) 75–82.

[34] M. Zhang, Z.S. Jin, J.W. Zhang, X.Y. Guo, J.J. Yang, W. Li, X.D. Wang, Z.J. Zhang, *J. Mol. Catal. A* 217 (2004) 203–210.

[35] Q.Y. Li, J.W. Zhang, Z.S. Jin, D.G. Yang, X.D. Wang, J.J. Yang, Z.J. Zhang, *Electrochem. Commun.* 8 (2006) 741–746.

[36] Q.Y. Li, X.D. Wang, Z.S. Jin, D.G. Yang, S.L. Zhang, X.Y. Guo, J.J. Yang, Z.J. Zhang, *J. Nanopart. Res.* 5 (2007) 951–957.

[37] W.P. Chen, X.Y. Guo, S.L. Zhang, Z.S. Jin, *J. Nanopart. Res.* 9 (2007) 1173–1180.

[38] C.X. Feng, Z.S. Jin, J.W. Zhang, Z.S. Wu, Z.J. Zhang, *Photochem. Photobiol.* 86 (2010) 1222–1229.

[39] Y. Wang, C.X. Feng, M. Zhang, J.J. Yang, Z.J. Zhang, *Appl. Catal. B* 100 (2010) 84–90.

[40] Y. Wang, C.X. Feng, M. Zhang, J.J. Yang, Z.J. Zhang, *Appl. Catal. B* 104 (2011) 268–274.

[41] C.X. Feng, G.G. Li, P.H. Ren, Y. Wang, X.S. Huang, D.L. Li, *Appl. Catal. B* 158–159 (2014) 224–232.

[42] X.D. Wang, J.J. Yang, H.Y. Yin, Z.J. Zhang, Z.S. Jin, *Photogr. Sci. Photochem.* 20 (2002) 424–428.

[43] G. Kresse, J. Hafner, *Phys. Rev. B* 47 (1993) 558–561.

[44] G. Kresse, J. Furthmüller, *Phys. Rev. B* 54 (1996) 11169–11186.

[45] P. Blöchl, *Phys. Rev. B* 50 (1994) 17953–17979.

[46] J.P. Perdew, Y. Wang, *Phys. Rev. B* 45 (1992) 13244–13249.

[47] J.P. Perdew, K. Burke, M. Ernzerhof, *Phys. Rev. Lett.* 77 (1996) 3865–3868.

[48] K.S. Yang, Y. Dai, B.B. Huang, *ChemPhysChem* 10 (2009) 2327–2333.

[49] S.L. Zhang, W. Li, Z.S. Jin, J.J. Yang, J.W. Zhang, Z.L. Du, Z.J. Zhang, *J. Solid State Chem.* 177 (2004) 1365–1371.

[50] F. Zuo, L. Wang, T. Wu, Z.Y. Zhang, D. Borchardt, P.Y. Feng, *J. Am. Chem. Soc.* 132 (2010) 11856–11857.

[51] G. Pecchi, P. Reyes, T. López, R. Goímez, A. Moreno, J.L.G. Fierro, A.J. Martínez-Arias, *Sol–Gel Sci. Technol.* 27 (2003) 205–214.

[52] R.J. Aasa, *Chem. Phys.* 52 (1970) 3919–3930.

[53] J.F. Zhu, F. Chen, J.L. Zhang, H.J. Chen, M. Anpo, *J. Photochem. Photobiol. A* 180 (2006) 196–204.

[54] C. Adán, A. Bahamonde, M. Fernández-García, A. Martínez-Arias, *Appl. Catal. B* 72 (2007) 11–17.

[55] J.F. Zhu, W. Zheng, B. He, J.L. Zhang, M. Anpo, *J. Mol. Catal. A* 216 (2004) 35–43.

[56] E.S. Gnanakumar, J. John, T. Raja, C.S. Gopinath, *J. Nanosci. Nanotechnol.* 13 (2013) 2682–2688.

[57] X.X. Zou, J.K. Liu, J. Su, F. Zuo, J.S. Chen, P.Y. Feng, *Chem. Eur. J.* 19 (2013) 2866–2873.